Woodstock: Interactive Modeling of Fungal Wood Decay

ZHANYU YANG*, Purdue University, USA
NIKOLAS A. SCHWARZ*, Kiel University, Germany
BOSHENG LI, Samsung, USA
DOMINIK L. MICHELS, KAUST, KSA
BEDRICH BENES, Purdue University, USA
SÖREN PIRK, Kiel University, Germany
WOJTEK PAŁUBICKI, Adam Mickiewicz University, Poland

Fig. 1. Woodstock framework simulates tree decomposition by modeling anisotropic moisture transport, fungal decay, and volumetric strand-based wood mechanics. The result is a coherent end-to-end breakdown – from drying- and decay-driven weakening to hollowing, cubical fragmentation, and debris accumulation.

Fungal wood decay is a complex biophysical phenomenon that involves the degradation of a variety of structural wood components, ranging from lignin and carbohydrates to defensive chemical agents. All these substrates serve as varying resources with different material properties that determine the rate of fungal propagation and the structural integrity and color of decaying wood. We propose a novel approach to simulate the dynamic interactions between the biological and mechanical components of wood decay, including fungal colonization, chemical defense, and moisture-driven fracture. We propose a novel volumetric representation of trees that includes grain-aligned mesh generation, internal moisture dynamics, and tissue-specific health states. Furthermore, we model the anisotropic diffusion, consumption, and resulting material failure caused by white and brown rot fungi. This allows simulating and rendering 3D volumetric decaying trees that realistically capture key aspects of the process, such as the progression of cuboid fracture patterns, the hollowing of trunks, and the effects of environmental moisture on structural stability.

CCS Concepts: • **Computing methodologies** → **Mesh geometry models**.

*Equal contribution.

Authors' Contact Information: Zhanyu Yang, yang2334@purdue.edu, Purdue University, 305 N University St., West Lafayette, IN, 47907-2021, USA; Nikolas A. Schwarz, nsch@informatik.uni-kiel.de, Kiel University, Christian-Albrechts-Platz 4, 24118 Kiel, Germany; Bosheng Li, li2343@purdue.edu, Samsung, 4052 Mahaila Ave. Unit B, San Diego, CA, 92122, USA; Dominik L. Michels, dominik.michels@kaust.edu.sa, KAUST, Thuwal 23955, KSA; Bedrich Benes, bbenes@purdue.edu, Purdue University, 305 N University St., West Lafayette, IN, 47907-2021, USA; Sören Pirk, soeren.pirk@gmail.com, Kiel University, 24118 Kiel, Germany; Wojtek Pałubicki, wojciech.palubicki@amu.edu.pl, Adam Mickiewicz University, 61-614, Poznań, Poland.

ACM 1557-7368/2026/7-ART155
https://doi.org/10.1145/3811376

ACM Reference Format:
Zhanyu Yang, Nikolas A. Schwarz, Bosheng Li, Dominik L. Michels, Bedrich Benes, Sören Pirk, and Wojtek Pałubicki. 2026. Woodstock: Interactive Modeling of Fungal Wood Decay. *ACM Trans. Graph.* 45, 4, Article 155 (July 2026), 17 pages. https://doi.org/10.1145/3811376

1 Introduction

Trees are complex living organisms, and their shape and color are influenced by external factors, among which fungi play an important yet often neglected role. Fungal decay is a ubiquitous natural process that significantly affects the wood of trees in forest ecosystems and in man-made structures. Specifically, the decomposition of wood is responsible for the annual release of gigatons of carbon and the creation of essential habitats for biodiversity [Boddy et al. 2008]. Wood decay is the progressive, often invisible degradation of lignified tissues that involves not only the consumption of structural components such as lignin and carbohydrates but also the dynamic interplay among moisture, chemical defenses, and fungal mycelium. These biological events lead to tree failure, property damage, and significant changes in forest stand dynamics. However, the mechanisms underlying the transition from a microscopic fungal infection to catastrophic structural collapse are complex and not fully understood. Therefore, to advance our understanding of the dynamics and progression of wood decay, we argue that it is critical to carefully simulate the feedback loops of fungal growth, material anisotropy, and the degradation of different tissue types. By creating realistic 3D simulations, it is possible not only to enable safety assessments but also to create applications for safety assessments and complex CG effects for movies or games.

A number of approaches have recently addressed the generation of more realistic models of trees and the related physical processes between vegetation and the environment. These methods range from developmental algorithms for detailed branching structures [Pałubicki et al. 2009; Runions et al. 2007] and environmental adaptation [Makowski et al. 2019] to the response of vegetation to wind [Habel et al. 2009; Pirk et al. 2014], and fracture [Li et al. 2025]. However, coupling intricate internal grain structures [Larsson et al. 2022] with complex reaction-diffusion systems, while also simulating the anisotropic shrinkage and fracture of wood, remains a challenging objective. To the best of our knowledge, no method has simulated the various types of distinct rot patterns — such as the cuboid cracking of brown rot or the fibrous stringiness of white rot — that are controlled by the breakdown of chemical components within the wood volume.

We propose a unified multi-scale representation for simulating 3D fungal decay. We generate 3D models of decaying wood based on a strand-based representation — each piece of wood is defined as a collection of strands and rod elements. Based on this representation, we can efficiently model the internal degradation of complex wooden structures. To simulate biological decomposition and mechanical failure, we develop a novel mathematical model for the propagation of fungi and moisture throughout the wooden tissue.

Our approach realistically captures decay patterns in different tissue contexts, ranging from the localized hollowing of heartwood to the surface degradation of sapwood. By including representations of tissue health (lignin and carbohydrates), our method captures plausible dynamics of structural loss and its behavior under external forces. Furthermore, we include comparisons with real-world decay observations that demonstrate that the emergent phenomena expressed with our simulations, such as immune-induced barrier effects, correspond to those observed in nature.

Fig. 1 shows a rendering of a complex decaying tree trunk created with our framework. The simulation parameters have been set to define an active brown-rot infection that consumes the carbohydrate components of the wood distributed throughout the scene.

In summary, the contributions of our paper are: (1) a novel coupled reaction-diffusion model that accounts for the distinct consumption patterns of white and brown rot fungi; (2) a moisture dynamics framework describing the impact of anisotropic shrinkage and chemical defense mechanisms on material integrity; (3) a method for coupling a mechanical model of wood with the fungal disease model to account for realistic wood decay.

2 Related Work

Tree Form: Understanding the shape and form of plants has been addressed by many computer graphics works as well as in developmental biology [Pałubicki et al. 2019]. The procedural description of tree form initially relied on formalisms such as L-systems, which can capture a wide range of botanical structures [Prusinkiewicz et al. 1993; Prusinkiewicz and Lindenmayer 1990]. However, manually deriving the generative rules for specific species remains a complex task. Consequently, recent approaches have sought to infer these rules automatically using machine learning techniques [Guo et al. 2020; Lee et al. 2024], or to reconstruct plant geometry directly from scanned data [Cieslak et al. 2024; Kałużny et al. 2024; Liu et al. 2021; Livny et al. 2011; Zhou et al. 2023]. To enhance biological realism, many methods leverage heuristic algorithms that simulate the competition for light and space, leading to the emergence of complex natural patterns [Pałubicki et al. 2022; Pałubicki et al. 2009; Pirk et al. 2012a; Runions et al. 2005]. These principles have been successfully extended to climbing plants [Benes and Millán 2002; Hädrich et al. 2017; Wong and Chen 2015] and inverse modeling frameworks that fit parameters to real-world observations [Niese et al. 2022; Šťava et al. 2014]. Procedural models are often parameterized to allow for artistic control [Lintermann and Deussen 1996; Longay et al. 2012], while sketch-based interfaces have been combined with developmental algorithms to guide high-level structure while delegating details to the procedural system [Anastacio et al. 2006; Benes et al. 2009; Chen et al. 2008; Neubert et al. 2007; Okabe et al. 2007; Tan et al. 2008; Wither et al. 2009].

Tree Dynamics: Beyond static morphology, *tree dynamics* address the interaction of vegetation with varying environmental conditions. Some methods model responses to biomechanical stress [Hädrich et al. 2020; Maggioli et al. 2023; Wang et al. 2017; Zhao and Barbič 2013], wind forces [Habel et al. 2009; Pirk et al. 2014, 2012b; Quigley et al. 2018; Shao et al. 2021], and the coordinated function of shoots and roots [Li et al. 2023]. These approaches typically couple a windfield representation with a physical response model to deform the tree geometry. More recently, the destructive interaction of wood with fire and combustion has also been explored [Kokosza et al. 2024; Pirk et al. 2017]. However, the *internal wood structure* has primarily

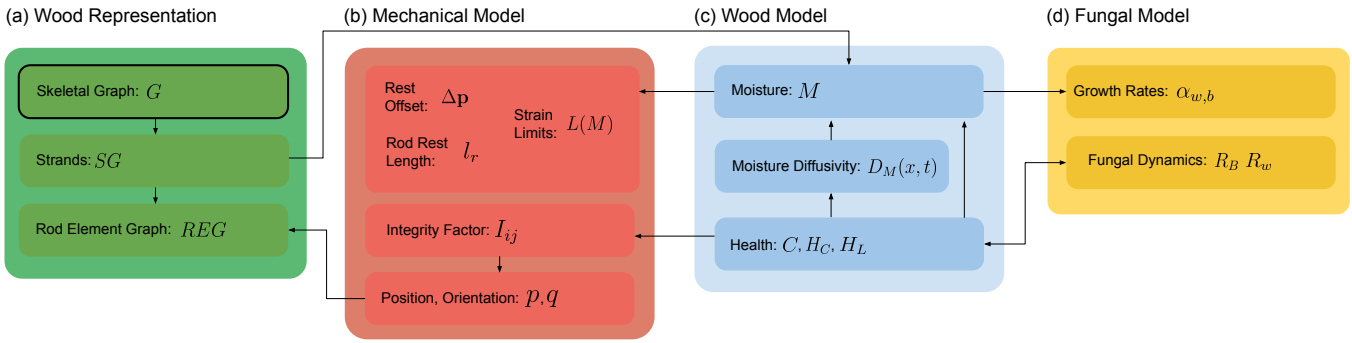

Fig. 2. (a) The input to our method is a skeletal graph G from which we construct a strand-based volumetric representation SG and the rod-element graph REG that defines the shared data structure for the wood, the mechanical, and the fungal model. (b) The mechanical model evolves rod states $(\mathbf{p}, \mathbf{q})$ with XPBD constraints on strand chains and REG connections, parameterized by rest offsets $\Delta\mathbf{p}$, rod rest lengths l_r, moisture-dependent strain limits $L(M)$, and an edge-wise integrity factor I_{ij}. (c) The wood model advances moisture M and host health state (C, H_c, H_l), with health-dependent moisture diffusivity $D_M(x,t)$. (d) The fungi model updates white- and brown-rot activities (R_w, R_b), whose growth is moisture-gated via $\alpha_{w,b}(M)$ and coupled to host condition. Arrows denote the principal couplings: moisture drives shrinkage and failure thresholds in mechanics; host state modulates moisture transport and mechanical integrity, and fungal activity both alters and is regulated by the wood state.

been studied from the perspective of surface appearance [Buchanan 1998; Larsson et al. 2022; Yang et al. 2019] or growth rings [Kratt et al. 2015; Larsson et al. 2025]. Successive instances of decaying trees have been used to enhance virtual ecosystems in [Peytavie et al. 2024]. Several recent works addressed the appearance of the internal wood structure [Larsson et al. 2024, 2022]. Our work builds upon strand-based representations [Hädrich et al. 2020; Holton 1994; Kleiberg et al. 2001; Li et al. 2025] and extends them with a physical framework for simulating structural tree degradation.

Rod Physics: We rely on rod physics to simulate the mechanical behavior of strands. Numerical methods for tree dynamics generally fall into two categories: volumetric discretization, which employs techniques like the finite element method on tetrahedral meshes [Kratt et al. 2015; Wang et al. 2013; Zhao and Barbič 2013], and centerline extraction, which models branches as connected curves. Our approach belongs to the latter. We utilize Cosserat rods, which model each branch as a one-dimensional continuum with embedded directors, enabling accurate simulation of bending, twisting, and stretching. Introduced in the context of graphics by Pai [2002], the Cosserat model has been widely adopted for slender structures such as fibers [Spillmann and Teschner 2007], nets [Spillmann and Teschner 2008], and hair [Bertails et al. 2006; Michels et al. 2017, 2015]. Kugelstadt and Schömer [2016] integrated this concept into the Position-Based Dynamics (PBD) framework, a formulation that has proven highly effective for simulating complex tree dynamics in recent years [Maggioli et al. 2023; Pirk et al. 2017; Shao et al. 2021]. Recently, Hsu et al. [2025] proposed a stable formulation for Cosserat rods, further advancing the robust simulation of slender structures and complementing the growing use of rod-based models in graphics.

Fungal Modeling and Simulation: Fungal modeling remains an under-explored area in computer graphics. Early work in this domain focused on the visual weathering of wood surfaces [Chen et al. 2005] or the propagation of lichen on stone substrates [Desbenoit et al. 2004], primarily for rendering purposes rather than structural simulation. In the biological sciences, the topology of mycelial networks has been modeled as a resource optimization process [Fricker et al. 2017], yet these methods do not account for the volumetric degradation of the host substrate. The mechanical consequences of decay are well-documented in arboriculture, where distinct rot types, such as the fibrous degradation of white rot versus the cubical fracture of brown rot, drastically alter the material properties of the wood [Schwarze et al. 2000]. Our work bridges these domains by coupling the biological propagation of fungi with the mechanical response of the strand-based wood volume.

3 Overview

Our main goal is to develop a novel volumetric framework to simulate fungal propagation through the wood and its changes. We build on the strand-based fracture framework of Li et al. [2025], which focuses on mechanically driven failure, and extend it to a coupled biophysical-mechanical model of wood decay. The system is organized into four coupled components (Fig. 2): (a) a strand-based *wood representation* built from a skeletal graph, (b) a *mechanical model* based on Cosserat rod physics and their volumetric couplings, (c) a *wood-state model* that advances moisture and host condition, and (d) a *fungi model* that advances white- and brown-rot activities under moisture- and host-limited growth.

The input is a skeletal graph G describing the tree topology, annotated with planar cross-section profiles at nodes. These profiles define a packed strand group SG (Fig. 3a-b). We resample strands into rod particles and rod segments and group consecutive particles with their connecting segment into *rod elements* (Fig. 3b). To couple strands volumetrically, we build the *rod element graph* (REG) by connecting nearby rod elements into *segment pairs* that represent volumetric connectivity (Fig. 3c). This REG is the shared data structure for both mechanics and biophysics (Fig. 2a): it defines the integration domain, neighborhood exchange, and the location where the fungal-mechanical feedback occurs.

The mechanical solver evolves rod-element states $(\mathbf{p}, \mathbf{q})$ under XPBD constraints on strand chains and REG connections (Fig. 2b). It is parameterized by per-edge rest offsets $\Delta\mathbf{p}$, strand-wise rod rest lengths l_r, moisture-dependent strain limits $L(M)$, and an edge-wise integrity factor I_{ij} that controls whether REG connections are enforced (Sec. 5-5.4). In our coupled setting, $L(M)$ and I_{ij} are not constant: they are updated from the wood-state and decay fields, enabling progressive weakening and fracture.

We store per-rod-element wood state variables on the same REG discretization (Fig. 2c): moisture M and host condition (C, H_c, H_l), i.e., chemical defenses C and health fractions for carbohydrates and lignin. Moisture transport is advanced by diffusion with volumetric source – sink terms (Eq. 15), and its effective diffusivity depends on tissue condition (Eq. 20). Moisture then drives shrinkage and failure thresholds in the mechanical model by updating rest quantities and limits (Eqs. 16 – 18), as summarized by the couplings in Fig. 2b–c.

White- and brown-rot activities (R_w, R_b) are advanced as reaction–diffusion processes on rod elements (Eqs. 8–9), with moisture controlled growth rates $\alpha_{w,b}(M)$ (Eq. 10) (Fig. 2d). Fungal activity consumes host substrates via the health dynamics (Eqs. 12–13) and induces defenses through Eq. 14. This closes the biophysical feedback loop in Fig. 2: fungal dynamics alter the wood state, the wood state modulates transport and growth, and the resulting condition fields update mechanical parameters $(L(M), I_{ij})$ that govern fracture and separation.

To support physically plausible post-failure behavior once REG connections are disabled, we additionally simulate contact between detached components using capsule-based repulsion (Eq. 4) and particle-wise friction (Eq. 7) (Sec. 5.4). This enables broken pieces to collide, separate, and settle into plausible debris configurations in our results.

4 Biological Background

Decay is typically initiated by an infection event such as wind damage, insect vectors, or root grafting. Once a fungus colonizes the host, it releases enzymes that break down cell walls and cause moisture levels to fluctuate, which – in turn – allows the mycelium to penetrate deeper into the wood volume [Brischke and Alfredsen 2020; Goodell 2020]. This process, known as colonization, can cause rapid degradation of structural integrity. The rot can then spread from heartwood to sapwood, and spores can be carried by the air to infect new wounds in other areas [North Carolina Forest Service 2005]. Another physical phenomenon that can contribute to the spread of decay is moisture transport.

As the fungus metabolizes the wood, it extracts metabolic water and transports moisture from the soil, creating conditions that favor further growth even in dry environments [Forest Products Laboratory 2021]. This can cause the decay to spread persistently and unpredictably, making it difficult to detect. The rate of wood decay also depends on the tree species, the environmental humidity, and the type of fungus, such as white rot or brown rot. *White rot fungi* tend to degrade both lignin and cellulose, resulting in a soft, fibrous texture. The selective consumption of lignin allows the remaining cellulose fibers to separate, leaving the wood with a stringy, bleached appearance. White rot may spread more thoroughly in

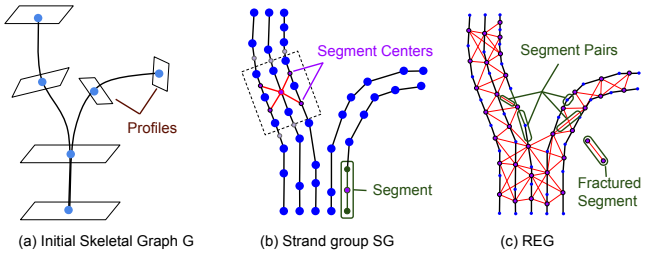

Fig. 3. (a) We start from a skeletal graph G annotated with planar cross-section profiles at nodes. (b) The profiles define a packed strand group SG, discretized into rod segments and their centers (simulation primitives). (c) We build the rod element graph (REG) by connecting nearby rod elements into segment pairs that represent volumetric connectivity; disconnecting these pairwise connections yields fractures and segment separations, which we render as wood splinters in our framework.

hardwoods, eventually reducing the wood to a soft, spongy mass that retains some tensile strength but loses compressive stability. *Brown rot fungi* can be highly destructive to structural stability, characterized by the rapid depolymerization of cellulose while leaving the lignin matrix largely intact.

The removal of carbohydrates causes the wood to shrink significantly upon drying, creating a complex pattern of cubical cross-checking cracks that can break with high brittleness and create significant structural hazards. This results in the wood crumbling into cubic chunks, a phenomenon often described as cubical rot, as shown in Fig. 4. *Wood defense mechanisms* play a crucial role in slowing these processes. Trees actively compartmentalize decay by depositing antifungal compounds, such as tannins and phenols, to wall off infected tissue. This creates a dynamic barrier where the rate of fungal advance is opposed by the tree's metabolic response. Finally, *moisture-induced failure* typically occurs when the compromised wood dries out. As the internal moisture content drops below the fiber saturation point, the anisotropic shrinkage of the wood exerts stress on the already weakened tissue. In decayed wood, the loss of structural bonds allows these shrinkage forces to propagate cracks along the grain and across the growth rings, leading to a structural collapse [Brischke and Alfredsen 2020].

5 Modeling Wood Mechanics

Our model operates on the strand-based representation introduced by Li et al. [2025, 2024]. The input is a skeletal graph G with planar cross-section profiles at nodes. A set of fixed-radius strands is generated as cubic B-splines whose control points are strand positions on these profiles. Strand positions on each profile are optimized with PBD to avoid collisions, which determines the branch cross-section packing and thus the volumetric distribution of strands.

From the initial strand set, we derive a randomly subdivided strand group SG used for physics and meshing. For each strand in SG, we sample *rod particles* $\mathbf{p}$ along the spline and connect consecutive particles into *rod segments*. A *rod element* is defined by two adjacent rod particles, their connecting rod segment, and the segment center. Rod elements are the simulation primitives that store kinematic state

(position, orientation, velocities) and material parameters (moisture, moduli, strain limits, rest length, and mass).

To couple strands volumetrically, we build a multi-connected REG. Its nodes are rod-element centers; REG edges are *rod element pairs* connecting nearby rod elements by minimum-distance paths, computed using the proximity-graph construction of Macklin et al. [2016]. Each rod element pair stores its own physical state (e.g., rest Darboux vector, positional offset) and integrity flags controlling whether coupling constraints are enforced. The mechanical simulation uses XPBD in two stages per time step. Stage 1 solves strand-wise Cosserat rod dynamics on each 1D chain of rod elements (one chain per strand). Stage 2 solves the multi-connected REG using XPBD connection constraints initialized from Stage 1.

5.1 Stage 1: Cosserat Rods on Strand Chains

For each strand chain, we integrate rod-element particle positions and segment orientations under external forces and torques as well as XPBD constraints. The constraint set includes distance constraints on rod particles, and Cosserat constraints for bending, torsion, shear/stretch, as well as collider constraints against external primitives (box, sphere, cylinder) following [Kugelstadt and Schömer 2016; Macklin et al. 2016]. In each solver iteration, predicted states $(\mathbf{p}', \mathbf{q}')$ are updated by projecting constraints $C_i(\mathbf{p}, \mathbf{q}) = 0$ using the XPBD multiplier update

$$\Delta\lambda = \frac{-C(\mathbf{p}, \mathbf{q})}{\nabla C^\top \mathbf{M}^{-1} \nabla C + \alpha}, \tag{1}$$

with compliance α. The output of Stage 1 is a per-rod-element estimate of position $\mathbf{p}$ and orientation $\mathbf{q}$ (and derived strains) that is used to initialize Stage 2.

5.2 Stage 2: XPBD on the REG

Stage 2 enforces volumetric coupling between neighboring strands by solving XPBD constraints on REG edges. For each connected pair of rod elements i, j, we enforce a positional connection constraint

$$C_{\text{connect}}(\mathbf{p}_i, \mathbf{p}_j) = \|\mathbf{p}_i - \mathbf{p}_j\| - \Delta\mathbf{p}, \tag{2}$$

where $\Delta\mathbf{p}$ is the stored rest offset for that pair. The same XPBD projection method is applied to the multi-connected graph using the Stage 1 estimates as initialization, which improves convergence compared to solving directly on the REG.

5.3 Failure and Connectivity Updates

Material failure is implemented by disabling constraints via integrity flags stored on rod element pairs. During each time step, we compute strains on rod element pairs (bend, torsion) and on rod elements (shear, stretch). If a rod element pair exceeds its bend or torsion limits, its bend or torsion integrity flags are set to false, preventing further enforcement of the corresponding coupling. If a rod element exceeds shear or stretch limits, the connectivity integrity for the affected connection is set to false, allowing separation while still permitting other constraints (e.g., partial sagging behavior) as in [Li et al. 2025]. After integrity updates, connected components are recomputed (e.g., via label propagation).

Fig. 4. A picture of a log affected by rot (left) and our simulation results (right). Our method successfully captures the characteristic orthogonal crack propagation and the resulting formation of distinct cubic chunks.

5.4 Contact Between Detached Components

Unlike Li et al. [2025], we simulate post-fracture contact using a local penalty model defined on *rod segments*. Each rod segment i is treated as a capsule whose centerline is the line segment between its two rod particles and whose radius is r_i. For a candidate pair of segments i and j, we compute the minimum capsule–capsule distance $\text{dist}(i, j)$ and the corresponding unit direction $\mathbf{n}_{ij}$ pointing from segment i to segment j. We define the penetration depth

$$\phi_{ij} = \max\big((r_i + r_j) - \text{dist}(i, j),\ 0\big), \tag{3}$$

and apply a quadratic penalty force to segment i,

$$\mathbf{F}_i = -k_{col}\, \phi_{ij}^2\, \mathbf{n}_{ij}, \tag{4}$$

where k_{col} is the collision stiffness. The equal-and-opposite force is applied to segment j.

Friction on the rod particles is computed to damp particle velocities in contact. Let $p_{i,k}$ denote rod particle $k \in \{1, 2\}$ of segment i, with velocity $\mathbf{v}_{i,k}$. For each particle–segment pair $(p_{i,k}, j)$, we compute the minimum distance $\text{dist}(p_{i,k}, j)$ from particle $p_{i,k}$ to the capsule of segment j, and the corresponding unit direction $\mathbf{n}_{ikj}$ pointing from $p_{i,k}$ to segment j. Using the penetration depth

$$\phi_{ikj} = \max\big((r_i + r_j) - \text{dist}(p_{i,k}, j),\ 0\big), \tag{5}$$

we define a penetration-based contact force

$$\Delta\mathbf{F}_{i,k} = -k_{col}\, \phi_{ikj}^2\, \mathbf{n}_{ikj}, \tag{6}$$

with the same stiffness k_{col}. We then apply a multiplicative damping update to the particle velocity,

$$\Delta\mathbf{v}_{i,k} = -\min\left(1,\ \mu_f \frac{\|\Delta\mathbf{F}_{i,k}\|\Delta t}{m_i\ \max(\|\mathbf{v}_{i,k}\|, \varepsilon)}\right)\mathbf{v}_{i,k}, \tag{7}$$

where μ_f is the friction coefficient, Δt is the simulation time step used in the XPBD integrator, m_i is the mass associated with segment i, and ε is a small constant to avoid division by zero.

6 Rot Dynamics Modeling

We simulate biological decay on the same rod-element discretization used by the mechanical solver (Sec. 5). Each rod element is associated with a local material frame $(\mathbf{e}_r, \mathbf{e}_t, \mathbf{e}_l)$ aligned with the radial, tangential, and longitudinal directions of wood. The biophysical processes described below are modeled in this local frame to support anisotropy, while the state itself is stored per rod element and exchanged with neighboring rod elements via REG adjacency.

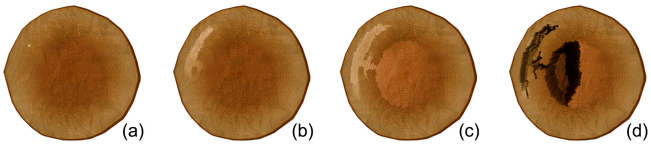

Fig. 5. Starting from a localized inoculation (a), the fungal front spreads preferentially along grain-aligned pathways (b). We model spatial anisotropy by modulating the transport operator with a 3D noise field that encodes specimen-specific weak regions (e.g., around branch junctions), yielding irregular, directionally biased colonization patterns over time (c, d).

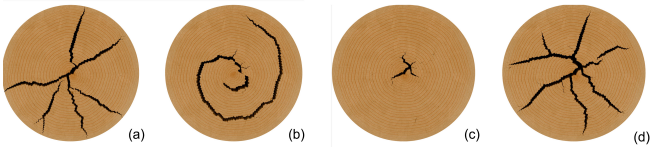

Fig. 6. Ablation study: When either radial or tangential material strength is artificially weakened, crack propagation becomes constrained to the corresponding direction, resulting in extreme fracture modes such as purely radial splitting or circumferential delamination (a, b). Under balanced radial and tangential material properties, shrinkage-induced stresses lead to non-uniform crack initiation and propagation. Crack competition and stress shielding result in a small number of dominant radial cracks, while secondary cracks remain or diminish over time, producing an asymmetric and realistic fracture pattern (c, d). The shrinkage gains in different directions are specified in Table 2.

To capture specimen-specific anisotropy beyond the global radial–tangential–longitudinal frame, we modulate the effective transport strength with a fixed spatial weak-point field $W(x) \in [0, 1]$. The 3D noise field W is evaluated in the local wood material frame (e_r, e_t, e_l). We implement W as a 3D Perlin noise function and use it to locally update diffusion and growth rates along different regions, producing irregular, directionally biased propagation consistent with observed decay pathways (Fig. 5).

For each rod element at position x and time t, we store: (1) fungal activity fields $R_w(x, t)$ and $R_b(x, t)$, representing the local *metabolic activity* of white-rot and brown-rot mycelium within the element. Both quantities are *dimensionless* and clamped to $[0, 1]$, where 0 denotes absence and 1 denotes local carrying-capacity saturation of fungal activity. (2) tissue state variables $H_c(x, t)$ and $H_l(x, t)$, representing the *remaining fraction* of structurally relevant carbohydrates (cellulose, hemicellulose) and lignin, respectively. Both are *dimensionless* and clamped to $[0, 1]$, where $H = 1$ denotes intact tissue and $H = 0$ denotes locally depleted substrate. (3) a chemical defense field $C(x, t)$, representing the *normalized local availability* of antifungal compounds (e.g., extractives or induced defenses) within the element. C is *dimensionless* and clamped to $[0, 1]$; it appears as a multiplicative inhibitor of fungal activity and saturates via $(1 - C)$, hence we model it as an efficacy index. (4) moisture content $M(x, t)$, represented as *gravimetric moisture content* (mass of water per dry mass of wood), with physical unit [kg/kg] (often reported as a percentage). We restrict $M \in [M_2, M_1]$, where M_2 and M_1 are the minimum and maximum admissible moisture contents used by the model.

White and brown rot are modeled as reaction–diffusion processes defined on rod elements, where local fungal activity increases through substrate-limited proliferation, decreases through chemical inhibition, and spreads through the wood volume.

All state variables in our model are normalized to represent physically meaningful quantities. Beyond numerical clamping, the continuous reaction–diffusion system itself guarantees this consistency: starting from valid initial conditions, the coupled dynamics preserve the intended bounds for all variables at all times. A concise proof is given in Appx. A.

For all parameters used in our model, we provide detailed descriptions and representative values/ranges in Table 3. The experiment-specific parameter changes used in the controlled studies are summarized in Table 2.

6.1 White Rot

White-rot activity R_w is defined as

$$\frac{\partial R_w}{\partial t} = \alpha_w(M)\, R_w(1 - R_w)\, (\lambda_l H_l + \lambda_c H_c)\, \frac{H_c}{K_c + H_c} - \beta_w\, C\, R_w + D_w \nabla^2 R_w\,, \tag{8}$$

The factor $R_w(1-R_w)$ implements local saturation of fungal activity, preventing unbounded growth and providing a carrying-capacity limit at $R_w = 1$. The scalar $\alpha_w(M)$ is introduced following a phenomenological approach to allow growth only within a prescribed moisture range, as defined in Eq.(10). Substrate limitation enters through $(\lambda_l H_l + \lambda_c H_c)$, a linear combination of lignin and carbohydrate availability (health fractions $H_l, H_c \in [0, 1]$), with weights λ_l, λ_c controlling their relative effect on growth rate.

We further include a carbohydrate accessibility factor $\frac{H_c}{K_c+H_c}$ (Michaelis–Menten form with half-saturation K_c) so that white rot can continue to act on lignin but cannot expand its population without sufficient accessible carbohydrates; this avoids growth in regions where carbohydrates are depleted while lignin remains. Chemical suppression is captured by $-\beta_w C R_w$, where $C \in [0, 1]$ is the defense efficacy field and β_w scales its inhibitory strength; the multiplicative form ensures inhibition vanishes if either fungus or defenses are absent. Finally, $D_w \nabla^2 R_w$ is the diffusion term that couples neighboring rod elements and represents spatial spread, with D_w controlling the propagation speed.

6.2 Brown Rot

Brown-rot activity R_b is defined as

$$\frac{\partial R_b}{\partial t} = \alpha_b(M)\, R_b(1 - R_b)\, H_c - \beta_b\, C\, R_b + D_b \nabla^2 R_b\,, \tag{9}$$

where $R_b(1-R_b)$ again enforces bounded local saturation and $\alpha_b(M)$ controls proliferation by moisture as before. In contrast to white rot, brown-rot growth is driven solely by carbohydrate availability H_c, reflecting that brown rot primarily depolymerizes carbohydrate-rich components while leaving most lignin as a modified residue. Defense inhibition $-\beta_b C R_b$ mirrors the white-rot term with a separate coefficient β_b, and $D_b \nabla^2 R_b$ controls spatial spread with diffusion coefficient D_b.

6.3 Moisture Dependence of Fungal Growth

We express moisture dependence by modulating the baseline growth rates α_{w0} and α_{b0} with a smooth windowing function of the local moisture content M:

$$\alpha_{w,b}(M) = \alpha_{w,b0}\,\psi\left(\frac{M - M_{\min}}{s_t}\right)\psi\left(\frac{M_{\max} - M}{s_t}\right), \tag{10}$$

where $\psi : \mathbb{R} \to [0,1]$ is the *smoothstep* function defined by

$$\psi(z) = \begin{cases} 0, & z \le 0, \\ 3z^2 - 2z^3, & 0 < z < 1, \\ 1, & z \ge 1. \end{cases} \tag{11}$$

For low moisture $M \ll M_{\min}$, the first factor is ≈ 0 and thus $\alpha_{w,b}(M) \approx 0$. For intermediate moisture $M_{\min}+s_t \lesssim M \lesssim M_{\max}-s_t$, both factors are ≈ 1 and $\alpha_{w,b}(M) \approx \alpha_{w,b0}$. For high moisture $M \gg M_{\max}$, the second factor is ≈ 0 and growth is suppressed again.

6.4 Tissue Health Dynamics

We represent substrate loss with two bounded health fractions: $H_c \in [0,1]$ for carbohydrates and $H_l \in [0,1]$ for lignin. Each depletion term is proportional to the corresponding fungal activity and the remaining substrate, yielding first-order consumption kinetics and ensuring that depletion slows as the substrate becomes scarce. Carbohydrate health evolves as

$$\frac{\partial H_c}{\partial t} = -\gamma_{cw}\,R_w\,H_c - \gamma_{cb}\,R_b\,H_c + \rho_c(1 - H_c)\,C, \tag{12}$$

where γ_{cw} and γ_{cb} control carbohydrate consumption by white and brown rot. The recovery term $\rho_c(1 - H_c)C$ increases H_c in proportion to defense availability C and the remaining "capacity" $(1 - H_c)$, so recovery saturates as $H_c \to 1$ and vanishes when $C = 0$. Lignin health evolves as

$$\frac{\partial H_l}{\partial t} = -\gamma_{lw}\,R_w\,H_l + \rho_l(1 - H_l)\,C, \tag{13}$$

where γ_{lw} controls lignin consumption by white rot and ρ_l controls the corresponding recovery term.

Together, Eqs. (12)–(13) provide independent spatial fields for carbohydrate and lignin depletion, allowing white and brown rot to produce distinct volumetric decay signatures: brown rot rapidly reduces H_c while leaving H_l largely intact, whereas white rot reduces both H_c and H_l. These health fields are the quantities we later couple to transport coefficients and mechanical integrity updates.

6.5 Defense Induction and Transport

Chemical defenses $C \in [0,1]$ are modeled as a bounded inhibitor field with induction, decay, and diffusion:

$$\frac{\partial C}{\partial t} = \kappa(R_w + R_b)\,\Pi(H)\,(1 - C) - \delta\,C + D_C\nabla^2 C, \tag{14}$$

where κ sets induction strength proportional to total fungal activity $R_w + R_b$, $(1 - C)$ enforces saturation, $\Pi(H)$ modulates inducibility from tissue condition (in our implementation, $\Pi(H) = H_c H_l$), δ is the natural decay rate, and D_C is the diffusion coefficient.

This defines spatially localized defense production via the $(R_w + R_b)$ term, as well as reduced defense capability in degraded tissue through $\Pi(H)$. Because C enters the fungal equations as a multiplicative inhibitor, the resulting coupling supports traveling-wave behavior in which fungal spread can be slowed or locally halted when defenses accumulate, while still permitting re-colonization once defenses decay through $-\delta C$.

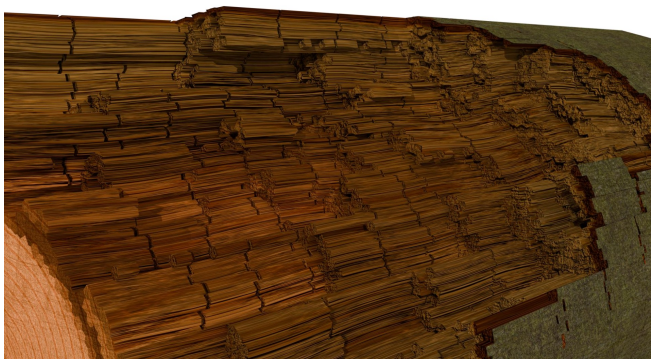

Fig. 7. Close-up of brown rot fungal decay in wood, highlighting the characteristic cuboid fracturing pattern caused by the fungus, leaving the wood dry, brittle, and cracked into distinct blocky segments.

Fig. 8. Lignin-degrading decay yields a smoother, more diffuse weakening pattern than brown rot: material loss spreads gradually through the volume, producing softened, stringy wood with an irregular surface rather than blocky fracturing.

6.6 Moisture Transport with Volumetric Exchange

Moisture content M evolves by diffusion and bounded source–sink terms:

$$\begin{aligned}\frac{\partial M}{\partial t} = \nabla\cdot(D_M\nabla M) + (M_1 - M)\,k_{\text{in}}\big(bd, H_c\big) \\ -(M - M_2)\,k_{\text{out}}\big(bd, H_c\big),\end{aligned} \tag{15}$$

where $M \in [M_2, M_1]$ is the gravimetric moisture content, $bd = bd(x)$ is the distance to the bark boundary at position x, and $k_{\text{in}}(\cdot)$, $k_{\text{out}}(\cdot)$ are source/sink rate functions. The factors $(M_1 - M)$ and $(M - M_2)$ make uptake vanish as $M \to M_1$ and loss vanish as $M \to M_2$, respectively. In our implementation, k_{in} is in the form of $k^0_{\text{in}}(1 - k^{in}_r \cdot bd)H_c$, k_{out} is in the form of $k^0_{\text{out}}(1 - k^{out}_r H_c)(bd_0 - bd)_+$.

7 Moisture-to-Mechanics Coupling

After updating the moisture field $M(x,t)$, we map it to mechanical rest quantities and strain limits used by the rod solver. Let $(\cdot)^+ = \max(\cdot, 0)$ and let M_0 denote the critical moisture threshold below which moisture-driven shrinkage and reduced failure or strain capacity are initiated.

For each REG edge (rod element pair), we scale its rest offset distance (the $\Delta\mathbf{p}$ term in Eq. 2) as

$$\Delta\mathbf{p} \;\leftarrow\; \Delta\mathbf{p}_0 \Big(1 - (M_0 - M)^+ S\Big), \tag{16}$$

where $\Delta\mathbf{p}_0$ is the default (healthy, wet) rest offset and S controls how strongly drying reduces this offset. When $M \geq M_0$, we have $(M_0 - M)^+ = 0$ and therefore $\Delta\mathbf{p} = \Delta\mathbf{p}_0$, i.e., no moisture-driven change is applied. When $M < M_0$, the factor $(M_0 - M)^+$ becomes positive and decreases $\Delta\mathbf{p}$, meaning the solver tries to keep neighboring rod elements closer together than in the wet state. Increasing S strengthens this effect (faster reduction of $\Delta\mathbf{p}$ for the same moisture deficit), which increases the internal constraint forces required to satisfy the shortened rest offsets and therefore promotes drying-induced deformation and failure. For each rod element along a strand, we update its rod rest length as

$$l_r \;\leftarrow\; l_{r0} \Big(1 - (M_0 - M)^+ s\Big), \tag{17}$$

where l_{r0} is the default (wet) rest length and s controls how strongly drying shortens the strand direction.

We additionally scale the XPBD strain limits (shear, stretch, bend, twist, and bundle) by a moisture-dependent factor

$$L(M) \;=\; L_0\, f(M - M_2)\,, \tag{18}$$

where L_0 denotes the corresponding default limit values in the healthy state, M_2 is the minimum admissible moisture content, and $f : \mathbb{R} \to [0,1]$ is a monotone mapping. In our implementation,

$$f(x) = \begin{cases} 0\,, & x \leq 0\,, \\ \left(\dfrac{x}{M_1 - M_2}\right)^{p_\ell}, & 0 < x < M_1 - M_2\,, \\ 1\,, & x \geq M_1 - M_2\,. \end{cases} \tag{19}$$

with exponent p_ℓ chosen per constraint type, and M_1 the maximum admissible moisture content. Increasing p_ℓ makes the reduction of $L(M)$ steeper near the dry end, so constraints reach their failure thresholds earlier under drying; decreasing p_ℓ produces a more gradual reduction of limits over the same moisture range.

To couple decay back into moisture transport, we make the moisture diffusivity depend on a scalar health aggregate $H(x,t)$ computed from (H_c, H_l):

$$D_M(x,t) = D_{M0}\big(1 + k_{DM}(1 - H(x,t))\big)\,, \tag{20}$$

where D_{M0} is the baseline diffusivity and $k_{DM} \geq 0$ controls sensitivity. When tissue is healthy ($H \approx 1$), we obtain $D_M \approx D_{M0}$; as decay progresses and H decreases, D_M increases linearly with $1 - H$. Larger k_{DM} amplifies this increase, accelerating moisture equalization in degraded regions relative to healthy wood.

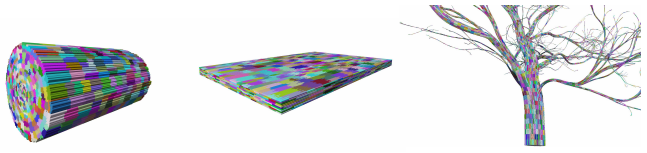

Fig. 9. Binary space partitioning in wood-local coordinates assigns each rod element a coarse cell ID (color), yielding controllable cuboid-sized regions for a board, a log, and a full tree; REG connections crossing cell boundaries are treated as potential weak planes to promote brown-rot cubical checking.

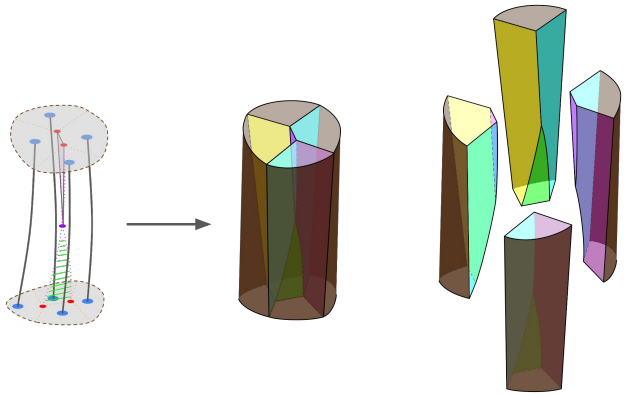

Fig. 10. We convert the strand discretization into a watertight surface partition by constructing a cross-section–consistent volumetric tessellation around strands; each resulting meshlet corresponds to a rod element and can be detached after connectivity failure, enabling fracture-aware rendering and interaction.

7.1 BSP-Based Prepatterning for Cubical Patterns

Brown rot often produces cubical patterns, in which separation occurs along approximately planar interfaces. To reproduce this macroscopic fragmentation pattern robustly at log and tree scale, we introduce a geometric prepattern that biases which volumetric connections in the REG are most susceptible to integrity loss under carbohydrate depletion.

Each rod element center x is mapped to wood-local coordinates (r, φ, s), where s is distance-to-root along the skeleton, and (r, φ) are polar coordinates in the local cross-section frame. We build a BSP tree over the normalized space $(\tilde{r}, \tilde{\varphi}, \tilde{s})$ and assign each rod element a leaf index groupID(i). Figure 11 shows the resulting cubical partitions (colored by groupID) for a board, a log, and a tree.

For each REG edge (i, j), we define

$$\theta_{ij} = \mathbb{I}\big[\text{groupID}(i) \neq \text{groupID}(j)\big],$$

so that edges crossing BSP cells are flagged as potential weak planes. These edges are not broken a priori; instead, θ_{ij} enters the integrity update (Eq. 21) to preferentially reduce connectivity across cell boundaries as H_c decreases, yielding stable cubical fragmentation while leaving the exact separation events to the XPBD failure dynamics. Figure 11 illustrates the effect of different BSP configurations on the resulting fracture morphology. The default setting in Fig. 11 (a) produces characteristic cubical fragmentation. Elongated BSP

cells in (b) introduce a stronger bias along the longitudinal direction, whereas larger cells in (c) lead to coarser and more block-like fracture patterns. When BSP prepatterning is removed entirely, as in Fig. 11 (d), the structure becomes more uniform and loses the distinctive cubical organization.

7.2 Integrity Update from Rot Patterns

After updating the biophysical fields, we convert tissue degradation into a scalar integrity value on each REG edge. For connected rod elements i and j, we define an integrity factor $I_{ij} \in [0, 1]$ as

$$I_{ij} = \Big(1 - \theta_{ij}\, k_c\, (1 - H_c)\Big)\, \Big(1 - k_l\, (1 - H_l)\Big), \tag{21}$$

where H_c and H_l denote the carbohydrate and lignin health values evaluated for the edge, and k_c and k_l control the strength of carbohydrate- and lignin-driven integrity loss, respectively.

The binary indicator $\theta_{ij} \in \{0, 1\}$ encodes the brown-rot cubical patterning derived from the BSP partitioning: $\theta_{ij} = 1$ if rod elements i and j belong to different BSP cells ($\text{group}(i) \neq \text{group}(j)$), and $\theta_{ij} = 0$ otherwise. Consequently, carbohydrate loss reduces integrity predominantly across BSP cell boundaries, while lignin loss reduces integrity independently of the BSP partition. The resulting integrity factor I_{ij} is applied to the corresponding REG connection by scaling its connection strength in the subsequent mechanical solve.

8 Implementation

All simulations are executed in our C++ framework, with physics, visualization, and real-time rendering implemented on the GPU using Vulkan for parallel acceleration. The online renderer operates directly on the simulated strand/rod state and the associated mesh representation, enabling continuous preview of fracture, separation, and decay progression. Unless stated otherwise, the online simulation results were produced on a workstation equipped with an Intel Core i9-10850K CPU, an NVIDIA GeForce RTX 3090 GPU, and 32 GB of RAM.

8.1 Meshing

We convert strand layouts into watertight meshlets suitable for fracture-aware rendering and interaction (Fig. 10). We treat each branch segment as a continuum of cross-sections indexed by a scalar parameter d_t, where d_t is the distance-to-root along the branch centerline. For every d_t, we evaluate all strand centerlines that pass through the branch at that location and project their intersection points into a local 2D cross-section frame attached to the branch (constructed by parallel transport along the centerline). This yields a family of moving 2D point sets $\mathcal{P}(d_t) = \{P_i(d_t)\}$, one point per strand, which can be viewed as a set of 2D parametric curves $P_i : [0, L] \to \mathbb{R}^2$ sampled through the cross-sectional profiles. $\mathcal{P}(d_t)$ induces a Voronoi partition at any $d_t \in [0, L]$, whose evolution we track using Guibas et al. [1992] to obtain boundaries for each strand such that the entire space is filled. To keep the implementation simple and robust, we represent each $P_i(d_t)$ piecewise linearly between successive cross-sections.

To bound the otherwise unbounded Voronoi partition induced by $\mathcal{P}(d_t)$, we compute a *kinetic alpha shape* [Kerber and Edelsbrunner 2013]: at each d_t, an alpha-complex is obtained by pruning the Delaunay triangulation of $\mathcal{P}(d_t)$ using a fixed radius threshold, and its outer polygonal boundary defines the cross-section contour. Rather than reconstructing this contour independently per slice, we traverse the branch by updating the triangulation and alpha-complex with discrete events as d_t advances under the piecewise-linear motion model; in practice, this reduces to processing local topological changes (e.g., edge flips) and membership changes of triangles in the alpha-complex. The resulting time-consistent boundary curves are then projected back to 3D in their corresponding cross-section planes and stitched along d_t to form a closed boundary surface for the entire branching structure. Finally, we tessellate the stitched boundary to obtain a watertight surface mesh that follows the strand distribution and remains stable under subsequent fracture and connectivity updates.

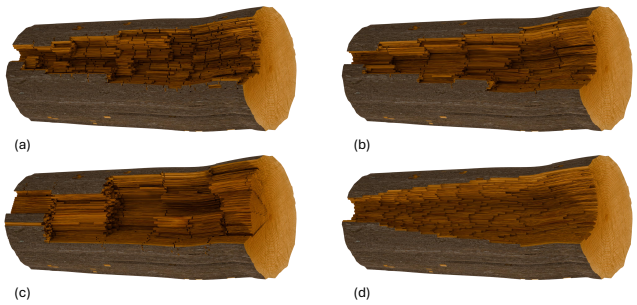

Fig. 11. Comparison of the fracture patterns under different BSP configurations: (a) default setting, (b) elongated cells (2.5× elongated along e_l), (c) large cells (16× larger volume), and (d) no BSP. Elongated cells introduce bias along the longitudinal direction, while larger cells lead to coarser patterns, and removing BSP introduces more uniform structures.

Fig. 12. A log progressively degraded by brown rot transitions from an intact log (top left) to cubical fragmentation and collapse (top right), followed by debris piling under our capsule-based contact and friction model. Increasing the fungal activity on one side yields finer fragments and a lower, more compact debris pile (bottom left, bottom right).

Algorithm 1: Coupled Rotting Simulation

Data: Skeletal graph G with profiles; model parameters; time steps $\Delta t_{\text{mech}}, \Delta t_{\text{bio}}$
Result: Rod states $(\mathbf{p}, \mathbf{q})$, REG connectivity/integrity, fields $(R_w, R_b, H_c, H_l, C, M)$

1 **Init:** build strands/rod elements and REG (Sec. 5); initialize $(\mathbf{p}, \mathbf{q})$ and rest data $(\Delta\mathbf{p}_0, l_{r0})$; initialize $(R_w, R_b, H_c, H_l, C, M)$ and inoculation;
2 Compute BSP groups and θ_{ij} (Sec. 7.1).
3 **for** $n = 1, \ldots, N$ **do**
  `// (1) Mechanics substeps`
4 **for** $k = 1, \ldots, N_{\text{mech}}$ **do**
5 Solve Cosserat strands + REG constraints (Eqs. (2));
6 Apply contact: repulsion (4), friction (7);
7 Update failure flags from strain limits (Sec. 5.3).
8 **end**
  `// (2) Biophysical update on rod elements (forward Euler on REG)`
9 Update R_w by (8) and R_b by (9);
10 Update H_c, H_l by (12)–(13) and C by (14);
11 Update moisture M by (15).
  `// (3) Coupling back to mechanics`
12 Update rest quantities by (16) and (17) (and limits $L(M)$ by (18));
13 Update edge integrity I_{ij} by (21) and apply it to REG connections.
14 **end**

8.2 Algorithm

Algorithm 1 summarizes our coupled biophysical–mechanical simulation on the REG discretization. In line 1, we construct the strand/rod-element representation and the REG (Sec. 5), and initialize the mechanical state $(\mathbf{p}, \mathbf{q})$ together with the associated rest data $(\Delta\mathbf{p}0, lr0)$ used by Stage 1/Stage 2 XPBD. We also initialize the biophysical fields per rod element, including inoculation seeds for (R_w, R_b) and initial material state (H_c, H_l, C, M). If cubical checking is enabled, line 2 computes the BSP group assignment and the boundary indicator θ_{ij} (Sec. 7.1), which later biases integrity loss in Eq. (21).

The outer loop in line 3 advances the simulation over macro steps. Within each macro step, lines 4–8 perform N_{mech} mechanical substeps at Δt_{mech} to resolve fast deformation and fracture dynamics. Specifically, line 5 solves strand-wise Cosserat dynamics (Stage 1) and volumetric coupling on the REG (Stage 2) using the XPBD constraints (Eq. 2). Line 6 applies post-fracture interactions through capsule repulsion and particle-wise friction (Eqs. 4–7). Line 7 updates integrity/failure flags by comparing computed strains to moisture-dependent strain limits (Sec. 5.3), enabling separation when limits are exceeded.

After the mechanics substeps, lines 9–11 advance the slower biophysical state at Δt_{bio} on rod elements with REG-neighborhood exchange. Line 9 updates fungal activities via the reaction–diffusion dynamics for white and brown rot (Eqs. 8 and 9). Line 10 updates tissue health and defenses using Eqs. (12)-(13) and Eq. (14), capturing substrate depletion, bounded recovery terms, and inhibitory coupling through C. Line 11 updates moisture using Eq. (15), which combines diffusion with bounded source–sink terms.

Finally, lines 12–13 apply the biophysical-to-mechanics coupling. Line 12 maps moisture to mechanical rest quantities and failure thresholds by updating the REG rest offsets and rod rest lengths (Eqs. 16 and 17) and the strain limits $L(M)$ (Eq. 18). Line 13 converts the current tissue state into an edge-wise integrity factor I_{ij} (Eq. 21), including the cubical-pattern prior through θ_{ij} when enabled, and applies it to the REG connections used in the next mechanical solve.

We advance the biophysical update (Eqs. 8-15) with an explicit forward-Euler step, and space is discretized on the REG using a graph Laplacian with an anisotropic Gaussian kernel; in our implementation, we update the coupled fields in a fixed order. Mechanics are integrated at the time scale of [Li et al. 2025] with a small time step ($\Delta t_{\text{mech}} \approx 0.005$–$0.01$ s) and multiple substeps per step, while decay and moisture evolve on a much slower effective time step (Δt_{bio} on the order of days). Practically, each iteration performs N_{mech} mechanical substeps followed by one biophysical update, which resolves fast fracture dynamics while accumulating slow decay over interactive time.

Fig. 13. Brown rot and white rot initiated at opposite ends of the log (rectangular areas). Brown rot preferentially degrades carbohydrate-rich sapwood, producing characteristic cubical fracture patterns, while white rot penetrates into lignin-rich heartwood, hollows the log, and produces a more diffuse degradation pattern.

8.3 Rendering

We use two rendering paths: an online renderer for interactive preview during simulation and an offline pipeline for final figures. During simulation, we render directly from the current rod/meshlet state, including detached components after connectivity failure, so users can inspect crack formation, separation, and rot evolution in real time. Each meshlet follows the simulated shrinkage of its corresponding segment.

For final-quality images, we export the fractured meshlets to Blender and render them with a standard PBR material. To preserve grain alignment under deformation and fracture, we evaluate all procedural texture coordinates in wood-local directions (radial, tangential, longitudinal). We modulate albedo and roughness with

coherent noise to reproduce natural heterogeneity, and we reuse the same fields for small-scale normal perturbations to add surface relief without increasing mesh complexity. The rot appearance is driven by the simulated fields: we blend color and roughness modifiers as functions of tissue health and moisture (e.g., H_c, H_l, M) to obtain consistent transitions from intact wood to degraded regions.

9 Result and Validation

We evaluate our coupled framework by demonstrating moisture-driven fracture behavior of the strand-based wood model, qualitative rot patterns and competition dynamics of white and brown rot, and emergent feedback between decay, moisture transport, and mechanical failure across board, log, and tree-scale scenarios.

9.1 Wood model

We first validate that our moisture-to-mechanics coupling reproduces characteristic shrinkage cracking and the expected sensitivity to directional strength. When moisture drops below the critical threshold M_0, we shorten the REG rest offsets and the strand rest lengths. This drives internal incompatibility: the XPBD solver must satisfy shorter rest states, increasing tensile/compressive stresses along the wood material frame and triggering fracture once strain limits are exceeded. Under balanced radial-tangential properties, this produces non-uniform crack initiation, yielding a small number of dominant radial cracks (Fig. 6c, d). If either radial or tangential resistance is artificially weakened, cracking becomes constrained to the corresponding direction, limiting failure modes to radial splitting or circumferential delamination (Fig. 6a, b).

We repeat the same full-tree simulation at two overall moisture settings and compare the resulting failure behavior (Fig. 16). All runs start from the same initial tree geometry and rot state; the only change is the initial moisture level of the wood. In our model, drier wood shrinks more and becomes more brittle, leading to internal stresses that build up earlier and the structure reaching breaking conditions sooner. This is why the drier case shows substantial branch loss and a partially collapsed configuration. As moisture increases, shrinkage effects weaken, and the wood tolerates larger deformations before breaking, so fewer branches detach, and the tree remains largely intact even when rot is present. In both cases, the decay process progressively hollows the trunk, forming a visible cavity that weakens the load-bearing core even when the outer shell remains connected.

9.2 Rotting Simulation

We evaluate the behavior of our coupled rot dynamics by qualitatively assessing decay signatures, inter-species competition, and anisotropic spread.

Figs. 7 and 8 compare the characteristic decay morphologies produced by our two rot models under identical geometry and discretization. In our method, the difference is driven by which state variables control mechanical integrity and where: brown rot primarily depletes carbohydrates, and this depletion is converted into patterned connectivity loss by the BSP-based weak-plane indicator θ_{ij} in the integrity update, causing REG connections to fail preferentially along prepatterned interfaces and producing blocky, cubical

Fig. 14. Evolution of wood decay of a cut tree trunk (top, left): Internal cracks emerge because of the moisture change (top, middle). The heartwood's low resistance makes it vulnerable to white rot, causing it to become hollow (top, right). Due to brown rot, the wood decays further (bottom, left) until it is fully affected by rot (bottom, center), and then it further decomposes (bottom, right).

Fig. 15. Initial moisture loss causes anisotropic shrinkage and fiber-aligned cracking in wood (left). The board is subsequently affected by fungal decay, leading to progressive internal deterioration (middle, right).

fragmentation. White rot, in contrast, reduces both H_c and lignin H_l through its coupled growth and consumption terms. Since lignin-driven softening enters the integrity update without θ_{ij}, weakening accumulates more isotropically across the REG, yielding a smoother, more diffuse volumetric deterioration rather than discrete cuboids.

Figure 13 demonstrates a bidirectional competition scenario in which brown rot and white rot inoculate opposite ends of the same log. The two decay modes propagate through different tissue regions and produce contrasting macroscopic outcomes: brown rot preferentially advances through carbohydrate-rich zones and promotes cubical fragmentation, whereas white rot penetrates into lignin-rich regions and causes progressive hollowing with a more diffuse degradation front. Our model also reproduces directionally biased spread consistent with wood's anisotropic transport properties. In Fig. 5, the inoculation at the upper-left produces an irregular, grain-aligned growth front rather than an isotropic radial expansion: activity advances predominantly in the tangential direction and only diffuses radially once it encounters a local weak spot, yielding the characteristic anisotropic decay pattern. Weak spots are defined by 3D noise fields where parameter values have been calibrated to simulate the spatial layout of branching points.

9.3 Fungal Decay and Mechanical Coupling

We demonstrate bidirectional coupling among mechanics, moisture, and decay across scales, from localized crack-rot interactions to

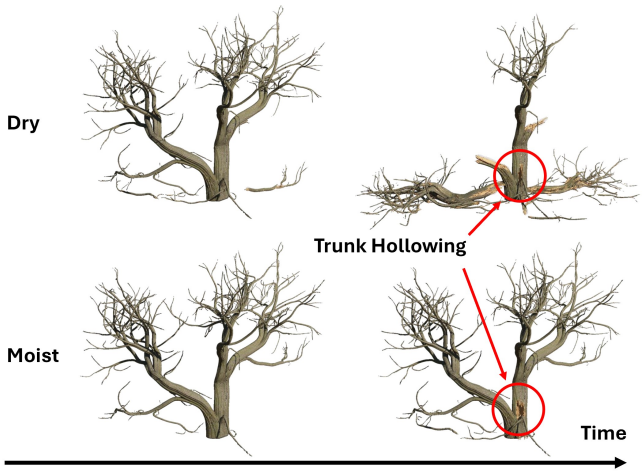

Fig. 16. Influence of environmental moisture. Both simulations start from the same initial state at Stage 1 of row 1, Fig. 19. Row 1: At a low moisture level, the fungal decay results in visible branch breakage due to hollowing of the branching structure. Row 2: At a high moisture level, branches do not fracture due to moisture effects alone. Even in the presence of fungal hollowing, the branches remain structurally intact. The cavity forms on the right branch due to stronger inoculation.

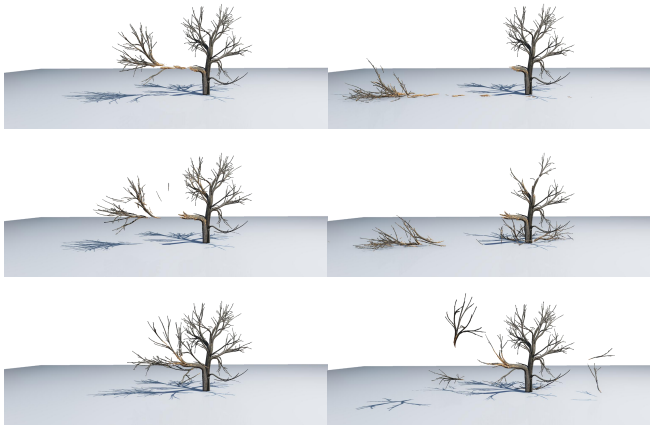

Fig. 17. A leftward force is applied to the left branch. When the tree's health is extremely low (Row 1), the branch immediately fragments into small pieces, preventing effective force transmission to the main branch, which remains largely unaffected. At a moderately low health level (Row 2), the weakened branch fractures early, but the applied force is transmitted through the trunk, causing pronounced oscillations in the main branch and leading to secondary breakage of smaller branches. When the tree is healthy (Row 3), a significantly larger force (10×) is required to break the branch. Instead of immediate failure, the branch undergoes strong oscillations and fractures dynamically, resulting in debris being scattered outward.

tree-scale collapse. Figure 14 shows an end-to-end trunk scenario in which moisture loss first induces internal cracking. As decay progresses, reduced resistance of the heartwood enables white rot to penetrate and hollow the trunk, after which brown rot further degrades the remaining load-bearing material, accelerating structural deterioration. After a fracture, detached components continue to interact through contact and friction, producing realistic debris arrangements. Figure 12 illustrates how progressive brown-rot weakening yields smaller debris and denser piles, with additional fungal activity on exposed fragments further reducing their size over time.

Figure 15 illustrates the biophysical feedback at the example of a wooden plank. Anisotropic shrinkage and fiber-aligned cracking emerge during drying, and are subsequently exploited by fungal decay, leading to progressive internal deterioration.

Figure 17 showcases how mechanical load transmission changes with decay by applying the same leftward pull to the left branch at three different temporal stages of fungal decay (rows). When the tree is severely degraded (Row 1), the pulled branch disintegrates almost immediately into small fragments; because the connection loses integrity early, a small force is transferred into the trunk, and the opposite branch remains nearly stationary. At intermediate health (Row 2), the fungal decay is more progressed in time, and the branch is structurally weakened. In this case, the main branch exhibits pronounced oscillations, resulting in secondary breakage of smaller branches as the structure moves. In the non-decayed case (Row 3), failure requires a much larger pull; instead of brittle breakup, the branch stores elastic energy, swings with large amplitude, and then fractures dynamically, producing a wider debris scatter.

Finally, Fig. 19 compares post-mortem evolution across three tree specimens with different geometry and species-specific material settings. Each row shows a different tree, while columns depict successive stages of decay and failure: the intact structure (Column 1), early drying-driven branch embrittlement and first breaks (Column 2), continued degradation with trunk hollowing and larger branch losses (Column 3), and late-stage collapse with debris accumulation (Column 4). To reflect species differences, we keep the fungal transport and growth parameters fixed across all rows (i.e., the same $\alpha_{w,b}(M)$ and $D_{w,b}$), and instead calibrate only the wood-response and coupling parameters that control drying, strength, and structural integrity, including the shrinkage gains S and s, the moisture threshold M_0, the moisture-to-failure mapping exponents p_ℓ, and the integrity coupling weights k_c and k_l. These choices yield distinct macroscopic outcomes: specimens with stronger drying response and lower strain tolerance lose peripheral branches earlier and accumulate larger debris fields, while more moisture-tolerant settings preserve larger connected components for longer despite ongoing fungal weakening.

Beyond parameter differences, the initial geometry strongly shapes the visible decay trajectory. Variations in branch density, trunk thickness, and cross-sectional distribution change the local moisture history and the accessible pathways for activity on the rod-element graph, which in turn alter where hollowing initiates and how weakening concentrates. In particular, slender, highly branched crowns promote earlier peripheral failures after drying, whereas thicker trunks delay global collapse but can exhibit more pronounced internal hollowing before the remaining scaffold fails.

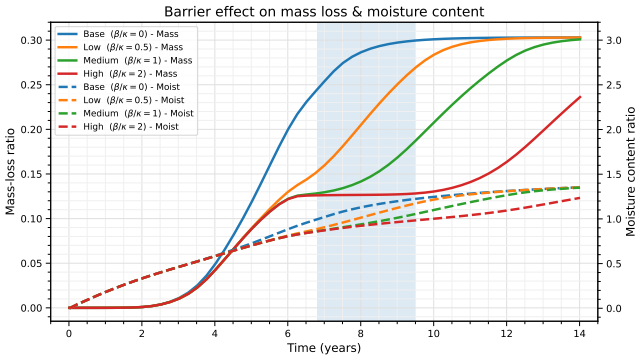

Fig. 18. Barrier effect on mass loss and moisture content predicted by our coupled decay model. We plot the mass-loss and moisture content over time for four inhibition-to-induction settings $\beta/\kappa \in \{0, 0.5, 1, 2\}$. Increasing β/κ strengthens the defense-mediated negative feedback, yielding a pronounced intermediate plateau (shaded) in which decay temporarily slows before resuming. The dashed graphs illustrate the dynamics of the moisture content ratio.

9.4 Barrier Effect

Laboratory block experiments report that fungal decay may exhibit *transient resistance*, i.e., a temporary slowdown of mass loss during intermediate degradation stages, attributed to structural or chemical barriers that reduce accessibility to cell-wall polymers [Bari et al. 2020]. We validate that our coupled reaction–diffusion system can reproduce this qualitative behavior through a parameter-space exploration of the defense coupling already present in our PDE model.

In Eqs. (8) and (9), fungal activity is inhibited by the local defense field through the multiplicative terms $-\beta_w C R_w$ and $-\beta_b C R_b$. In Eq. (14), defenses are induced proportionally to total fungal activity via $\kappa(R_w + R_b)$ and saturate by $(1 - C)$. Increasing the effective *inhibition-to-induction* ratios β_w/κ and β_b/κ strengthens the negative feedback loop, which can transiently pin the reaction front and reduce the net consumption rates of H_c and H_l over a range of intermediate tissue states. This emergently produces a barrier-like regime in our simulation.

Figure 18 shows the resulting mass-loss trajectories for increasing barrier strength. As the ratios $\beta_{w,b}/\kappa$ increase, the model exhibits an increasingly pronounced intermediate plateau, followed by renewed acceleration once defenses decay in Eq. (14).

We convert our health state variables to obtain an approximation of mass loss using $1 - [(H_l + k\,H_c)/(1 + k)]$ with $k = 2.5$, weighting carbohydrates relative to lignin. We define the moisture content ratio as $[(M - M_2)(1+k)\cdot l]/[(M_1 - M_2)(H_l + k\,H_c)]$, where l denotes the moisture-to-dry-mass ratio when the internal moisture reaches its maximum in the wood tissue prior to decay ($l = 1$). The qualitative plateau behavior in Fig. 18 is consistent with the transient resistance reported experimentally [Bari et al. 2020]. Absolute time alignment is not expected because the experiments use small blocks in direct contact with active mycelium under highly favorable conditions, whereas our simulations run at the scale of individual logs.

9.5 Spatial and Temporal Sensitivity Analysis

We perform a lightweight parameter value sensitivity analysis with respect to two numerical choices: the spatial discretization and the timestep. Figure 20 compares the default rod sampling with discretizations that are two and four times sparser. As expected, reducing the sampling resolution changes the local connectivity of the REG and the geometric detail of the resulting fracture surfaces. Nevertheless, the main qualitative behaviors remain consistent across all three settings: moisture loss still produces internal cracking, and the subsequent decay stage still yields the same overall patterns of rotting and fragmentation.

We also assess timestep sensitivity by comparing rendered states obtained with the default timestep and with a timestep reduced by 50%. Using SSIM on the rendered images, we obtain similarity scores of 0.9984 for the cracking state in Fig. 20 (b) and 0.9868 for the advanced degraded state in Fig. 20 (c).

10 Discussion and Limitations

Our method explores new ground by coupling a detailed strand mechanics model with spatial fungal spread, moisture transport, and a bounded host-state model on the same rod-element discretization. This coupling produces distinct, controllable macroscopic decay behaviors (e.g., hollowing for white rot and blocky fragmentation for brown rot), but it is designed for visual plausibility and interactive stability rather than species-calibrated wood research. In particular, decay does not explicitly simulate microstructural collapse, density changes, or void formation; instead, it acts through moisture-driven updates of rest quantities and strain limits, and through integrity weakening of REG connections.

Our formalization of choice for all biophysical equations is phenomenological in nature rather than directly deriving equations from first principles. We designed our set of equations as a minimal descriptive model: each term was introduced only when needed to reproduce a specific observed macroscopic behavior, such as barrier effects, moisture-driven differences, or distinct white-rot and brown-rot patterns. The main practical limitations follow from discretization, time stepping, and contact handling. Transport and integrity updates are resolved per rod element via REG adjacency, so strand density and rod-element spacing set the effective spatial resolution. Biophysical fields are advanced using an explicit forward-Euler update, and our mechanics and biology operate on different step sizes; this supports interactive runs but does not provide a calibrated mapping from iterations to real time. We report runtimes for the experiments depicted in the figures in Table 1 of Appendix C. Runtime differences across examples mainly stem from differences in strand and segment counts and the resulting number of REG connections and contact pairs. Finally, post-fracture interaction uses a local penalty contact model with capsule repulsion and particle-wise friction without continuous collision detection, so very fast fragments may still tunnel or jitter in extreme cases.

11 Conclusion

In this work, we presented an interactive framework for simulating fungal wood decay that enables the simulation of biological processes, moisture transport, and mechanical failure based on a

Fig. 19. Temporal development of different tree species after death. The tree is initially structurally intact (Column 1). After death, exposed branches rapidly lose moisture, becoming brittle and prone to breakage (Column 2). Meanwhile, anisotropic fungal activity primarily attacks heartwood, hollowing the trunk and further reducing overall structural stiffness, which increases the likelihood of branch failure (Column 3). Continued fungal decomposition ultimately weakens the remaining structure, leading to eventual structural collapse and further degradation (Column 4).

volumetric representation of trees. By modeling white rot and brown rot as distinct reaction-diffusion systems and embedding their effects directly into a strand-based mechanical solver, our approach captures characteristic decay phenomena such as cubical cracking, fibrous degradation, hollowing, and moisture-induced fracture.

A key contribution of our work is the bidirectional feedback loop between biology and mechanics: fungal activity and tissue health dynamically influence material integrity, while – in turn – mechanical damage and moisture redistribution affect biological propagation. This coupling enables emergent behavior that describes real-world decay patterns, while remaining efficient enough for interactive authoring and artistic control.

There are several promising directions for future work. For one, extending the biological model to include additional decay agents such as soft rot, insects, or microbial competition would further enrich realism. Second, a more physics-centric generation of cubical fracture patterns that emerge from material anisotropy and stress rather than procedural partitioning remains an open challenge. Finally, integrating data-driven parameter estimation from scanned or measured decay specimens could improve predictive accuracy and broaden applicability beyond visual simulation. We believe our framework represents an important step toward biologically informed modeling of tree degradation, with potential impact in visual effects, games, digital forestry, and ecological simulation.

Acknowledgments

This work was supported in part by the U.S. NSF under awards No. 2412928, 2506783, 2309564, and 2417510. Any opinions, findings, and conclusions or recommendations expressed in this material are those of the author(s) and do not necessarily reflect those of the National Science Foundation. This work is based upon efforts supported by the USDA-NIFA grants 2024-67021-42879 and 2023-08563. The views and conclusions contained herein are those of the authors and should not be interpreted as representing the official policies, either

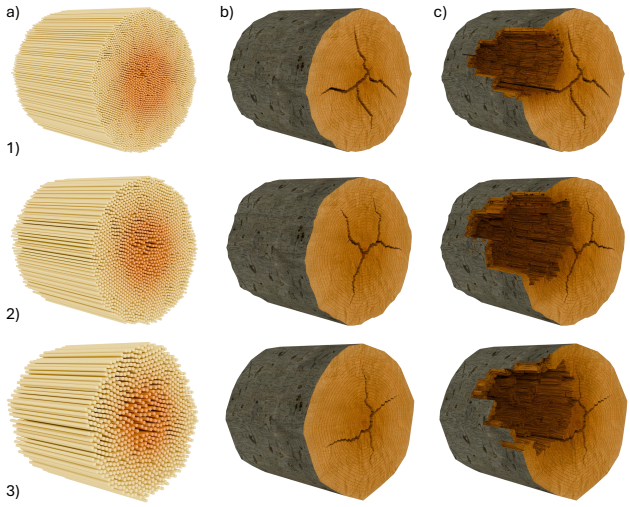

Fig. 20. Examples of varying spatial discretizations. Rows show the default setting (1), a two-times-sparser discretization (2), and a four-times-sparser discretization (3). All dynamic simulations consistently preserve the essential cracking and rotting dynamics.

expressed or implied, of the U.S. Government or NRCS. The U.S. Government is authorized to reproduce and distribute reprints for governmental purposes notwithstanding any copyright annotation therein. This work is also supported by ERC grant #101170158 - WildfireTwins.

References

F. Anastacio, M. C. Sousa, F. Samavati, and J. A. Jorge. 2006. Modeling Plant Structures Using Concept Sketches *(NPAR '06)*. ACM, 105–113.

E. Bari, G. Daniel, N. Yilgor, J. S. Kim, M. A. Tajick-Ghanbary, A. P. Singh, and J. Ribera. 2020. Comparison of the Decay Behavior of Two White-Rot Fungi in Relation to Wood Type and Exposure Conditions. *Microorganisms* 8, 12 (2020). https://doi.org/10.3390/microorganisms8121931

B. Benes, N. Andrysco, and O. Šťava. 2009. Interactive Modeling of Virtual Ecosystems. In *Proceedings of the Fifth Eurographics Conference on Natural Phenomena (NPH'09)*. Eurographics Association, Goslar, DEU, 9–16.

B. Benes and E. Millán. 2002. Virtual Climbing Plants Competing for Space. In *IEEE Proceedings of the Computer Animation 2002*. IEEE Computer Society, 33–42.

F. Bertails, B. Audoly, MP. Cani, B. Querleux, F. Leroy, and J. Lévêque. 2006. Super-Helices for Predicting the Dynamics of Natural Hair. *ACM Trans. on Graph.* (2006).

L. Boddy, J. C. Frankland, and P. Van West. 2008. Ecology of saprotrophic basidiomycetes. In *Ecology of saprotrophic basidiomycetes*. Elsevier.

C. Brischke and G. Alfredsen. 2020. Wood-water relationships and their role for wood susceptibility to fungal decay. *Applied Microbiology and Biotechnology* 104 (2020), 3781–3795. https://doi.org/10.1007/s00253-020-10479-1

J. W. Buchanan. 1998. Simulating wood using a voxel approach. In *CGF*, Vol. 17. 105–112.

X. Chen, B. Neubert, Y.-Q. Xu, O. Deussen, and S. B. Kang. 2008. Sketch-Based Tree Modeling Using Markov Random Field. *ACM Transactions on Graphics* 27, 5, Article 109 (Dec. 2008).

Y. Chen, L. Xia, T.-T. Wong, X. Tong, H. Bao, B. Guo, and H.-Y. Shum. 2005. Visual simulation of weathering by γ-ton tracing. *ACM Trans. Graph.* 24, 3 (July 2005), 1127–1133. https://doi.org/10.1145/1073204.1073321

M. Cieslak, U. Govindarajan, A. Garcia, A. Chandrashekar, T Hädrich, A. Mendoza-Drosik, D. L. Michels, S. Pirk, C.-C. Fu, and W. Pałubicki. 2024. Generating Diverse Agricultural Data for Vision-Based Farming Applications. *IEEE CVPR Workshop: Vision for Agriculture* (2024).

B. Desbenoit, E. Galin, and S. Akkouche. 2004. Simulating and modeling lichen growth. In *Computer Graphics Forum*, Vol. 23. Wiley Online Library, 341–350.

N. Fenichel and J. K. Moser. 1971. Persistence and smoothness of invariant manifolds for flows. *Indiana University Mathematics Journal* 21, 3 (1971), 193–226.

Forest Products Laboratory. 2021. *Wood Handbook—Wood as an Engineering Material: Chapter 14, Biodeterioration of Wood*. Technical Report FPL-GTR-282. U.S. Department of Agriculture, Forest Service, Forest Products Laboratory.

M. D. Fricker, L. L. M. Heaton, N. S Jones, and L. Boddy. 2017. The mycelium as a network. *Microbiology Spectrum* 5, 3 (2017), 5–3.

B. Goodell. 2020. Fungal Degradation of Wood: Emerging Data, New Insights and Changing Perceptions. *Coatings* 10, 12 (2020), 1210. https://doi.org/10.3390/coatings10121210

L. J. Guibas, Joseph S. B. Mitchell, and Thomas Roos. 1992. Voronoi diagrams of moving points in the plane. In *Graph-Theoretic Concepts in Computer Science*, Gunther Schmidt and Rudolf Berghammer (Eds.). Springer Berlin Heidelberg, Berlin, Heidelberg, 113–125.

J. Guo, H. Jiang, B. Benes, O. Deussen, X. Zhang, D. Lischinski, and H. Huang. 2020. Inverse Procedural Modeling of Branching Structures by Inferring L-Systems. *ACM Trans. Graph.* 39, 5, Article 155 (June 2020), 13 pages.

R. Habel, A. Kusternig, and M. Wimmer. 2009. Physically Guided Animation of Trees. *Computer Graphics Forum (Proceedings EUROGRAPHICS 2009)* 28, 2 (March 2009), 523–532.

T. Hädrich, B. Benes, O. Deussen, and S. Pirk. 2017. Interactive Modeling and Authoring of Climbing Plants. *Comput. Graph. Forum* 36, 2 (May 2017), 49–61.

T. Hädrich, J. Scheffczyk, W. Pałubicki, S. Pirk, and D. L. Michels. 2020. Interactive Wood Fracture. In *Eurographics/ ACM SIGGRAPH Symposium on Computer Animation - Posters*. https://doi.org/10.2312/SCA.20201215

M. Holton. 1994. Strands, Gravity and Botanical Tree Imagery. *CGF* 13(I) (1994), 57–67.

J. Hsu, T. Wang, K. Wu, and C. Yuksel. 2025. Stable Cosserat Rods. In *Proceedings of the Special Interest Group on Computer Graphics and Interactive Techniques Conference Conference Papers (SIGGRAPH Conference Papers '25)*. Association for Computing Machinery, New York, NY, USA, Article 75, 10 pages. https://doi.org/10.1145/3721238.3730618

J. Kałużny, Y. Schreckenberg, K. Cyganik, P. Annighöfer, S. Pirk, D. Michels, M. Cieslak, F. Assaad, B. Benes, and W. Pałubicki. 2024. LAESI: Leaf Area Estimation with Synthetic Imagery. *IEEE CVPR Workshop: Synthetic Data for Computer Vision* (2024).

M. Kerber and H. Edelsbrunner. 2013. 3D kinetic alpha complexes and their implementation. In *Proceedings of the Meeting on Algorithm Engineering & Experiments* (New Orleans, Louisiana). Society for Industrial and Applied Mathematics, USA, 70–77.

E. Kleiberg, H. Van de Wetering, and J. Van Wijk. 2001. Botanical visualization of huge hierarchies. In *IEEE INFOVIS*. IEEE, 87–94.

A. Kokosza, H. Wrede, D. Esparza, M. Makowski, D. Liu, D. Michels, S. Pirk, and W. Pałubicki. 2024. Scintilla: Simulating Combustible Vegetation for Wildfires. *ACM Transactions on Graphics* 43 (04 2024).

J. Kratt, M. Spicker, A. Guayaquil, M. Fiser, S. Pirk, O. Deussen, J. C. Hart, and B. Benes. 2015. Woodification: User-Controlled Cambial Growth Modeling. *Comput. Graph. Forum* 34, 2 (May 2015), 361–372.

T. Kugelstadt and E. Schömer. 2016. Position and Orientation Based Cosserat Rods. In *Eurographics/ ACM SIGGRAPH SCA*.

M. Larsson, T. Ijiri, I. Shen, H. Yoshida, A. Shamir, and T. Igarashi. 2024. Learned Inference of Annual Ring Pattern of Solid Wood. In *CGF*.

M. Larsson, T. Ijiri, H. Yoshida, J. A. J. Huber, M. Fredriksson, O. Broman, and T. Igarashi. 2022. Procedural texturing of solid wood with knots. *ACM Trans. Graph.* 41, 4, Article 45 (July 2022), 10 pages. https://doi.org/10.1145/3528223.3530081

M. Larsson, H. Yamaguchi, E. Pajouheshgar, I.-C. Shen, K. Tojo, C.-M. Chang, L. Hansson, O. Broman, T. Ijiri, A. Shamir, W. Jakob, and T. Igarashi. 2025. The Mokume Dataset and Inverse Modeling of Solid Wood Textures. *ACM Trans. Graph.* 44, 4, Article 162 (July 2025), 18 pages. https://doi.org/10.1145/3730874

J. J. Lee, B. Li, and B. Benes. 2024. Latent L-Systems: Transformer-Based Tree Generator. *ACM Trans. Graph.* 43, 1, Article 7 (2024), 16 pages.

B. Li, J. Klein, D. L. Michels, B. Benes, S. Pirk, and W. Pałubicki. 2023. Rhizomorph: The Coordinated Function of Shoots and Roots. *ACM Trans. Graph.* 42, 4, Article 59 (2023), 16 pages.

B. Li, N. Schwarz, W. Pałubicki, S. Pirk, D. L. Michels, and B. Benes. 2025. Stressful Tree Modeling: Breaking Branches with Strands. In *SIGGRAPH Conference Conference Papers (SIGGRAPH Conference Papers '25)*. Association for Computing Machinery, New York, NY, USA, Article 157, 11 pages. https://doi.org/10.1145/3721238.3730745

B. Li, N. A. Schwarz, W. Pałubicki, S. Pirk, and B. Benes. 2024. Interactive Invigoration: Volumetric Modeling of Trees with Strands. *ACM Trans. Graph.* 43, 4, Article 146 (2024).

B. Lintermann and O. Deussen. 1996. Interactive Modelling and Animation of Branching Botanical Structures. In *Computer Animation and Simulation'96 (Springer Computer Science)*. Springer–Verlag Wien New York, 139–151.

Z. Liu, K. Wu, J. Guo, Y. Wang, O. Deussen, and Z. Cheng. 2021. Single Image Tree Reconstruction via Adversarial Network. *Graphical Models* 117 (2021), 101115.

Y. Livny, S. Pirk, Z. Cheng, F. Yan, O. Deussen, D. Cohen-Or, and B. Chen. 2011. Texture-lobes for tree modelling. *ACM Trans. Graph.* 30, 4, Article 53 (July 2011), 10 pages. https://doi.org/10.1145/2010324.1964948

S. Longay, A. Runions, F. Boudon, and P. Prusinkiewicz. 2012. TreeSketch: Interactive Procedural Modeling of Trees on a Tablet. In *Proceedings of the International*

Symposium on Sketch-Based Interfaces and Modeling (SBIM '12). 107–120.
M. Macklin, M. Müller, and N. Chentanez. 2016. XPBD: position-based simulation of compliant constrained dynamics. In *Proceedings of the 9th International Conference on Motion in Games (MIG '16)*. ACM, 49–54.
F. Maggioli, J. Klein, T. Hädrich, E. Rodolà, W. Pałubicki, S. Pirk, and D. L. Michels. 2023. A Physically-inspired Approach to the Simulation of Plant Wilting. In *SIGGRAPH Asia 2023 Conference Papers (SA '23)*. ACM, Article 66, 8 pages.
M. Makowski, T. Hädrich, J. Scheffczyk, D. L. Michels, S. Pirk, and W. Pałubicki. 2019. Synthetic Silviculture: Multi-Scale Modeling of Plant Ecosystems. *ACM Trans. Graph.* 38, 4, Article 131 (July 2019), 14 pages. https://doi.org/10.1145/3306346.3323039
D. L. Michels, V. T. Luan, and M. Tokman. 2017. A stiffly accurate integrator for elastodynamic problems. *ACM Trans. Graph.* 36, 4, Article 116 (jul 2017), 14 pages.
D. L. Michels, J. P. T. Mueller, and G. A. Sobottka. 2015. A physically based approach to the accurate simulation of stiff fibers and stiff fiber meshes. *Computers & Graphics* 53 (2015), 136–146.
B. Neubert, T. Franken, and O. Deussen. 2007. Approximate Image-Based Tree-Modeling using Particle Flows. *ACM Trans. Graph. (Proc. of SIGGRAPH 2007)* 26, 3 (2007).
T. Niese, S. Pirk, M. Albrecht, B. Benes, and O. Deussen. 2022. Procedural Urban Forestry. *ACM Trans. Graph.* 41, 2, Article 20 (March 2022), 18 pages.
North Carolina Forest Service. 2005. Forest Pathology (extension/primer PDF): disease cycle, transmission, infection courts, vectors, and spores.
M. Okabe, S. Owada, and T. Igarashi. 2007. Interactive Design of Botanical Trees Using Freehand Sketches and Example-based Editing. In *ACM SIGGRAPH Courses* (San Diego, California). ACM, Article 26.
D. K. Pai. 2002. STRANDS: Interactive Simulation of Thin Solids using Cosserat Models. *CGF* 21, 3 (2002), 347–352.
W. Pałubicki, M. Makowski, W. Gajda, T. Hädrich, D. L. Michels, and S. Pirk. 2022. Ecoclimates: Climate-response Modeling of Vegetation. *ACM Trans. Graph.* 41, 4, Article 155 (July 2022), 19 pages. https://doi.org/10.1145/3528223.3530146
W. Pałubicki, K. Horel, S. Longay, A. Runions, B. Lane, R. Měch, and P. Prusinkiewicz. 2009. Self-Organizing Tree Models for Image Synthesis. *ACM Trans. Graph.* 28, 3, Article 58 (jul 2009), 10 pages. https://doi.org/10.1145/1531326.1531364
W. Pałubicki, A. Kokosza, and A. Burian. 2019. Formal description of plant morphogenesis. *Journal of Experimental Botany* 70, 14 (07 2019), 3601–3613.
A. Peytavie, J. Gain, E. Guerin, O. Argudo, and E. Galin. 2024. Deadwood: Including disturbance and decay in the depiction of digital nature. *ACM Transactions on Graphics* 43, 2 (2024), 1–19.
S. Pirk, M. Jarząbek, T. Hädrich, D. L. Michels, and W. Pałubicki. 2017. Interactive Wood Combustion for Botanical Tree Models. *ACM Trans. Graph.* 36, 6, Article 197 (2017), 197:1–197:12 pages.
S. Pirk, T. Niese, O. Deussen, and B. Neubert. 2012a. Capturing and Animating the Morphogenesis of Polygonal Tree Models. *ACM Trans. Graph.* 31, 6, Article 169 (2012), 169:1–169:10 pages.
S. Pirk, T. Niese, T. Hädrich, B. Benes, and O. Deussen. 2014. Windy Trees: Computing Stress Response for Developmental Tree Models. *ACM Trans. Graph.* 33, 6, Article 204 (Nov. 2014). https://doi.org/10.1145/2661229.2661252
S. Pirk, O. Stava, J. Kratt, M. A. M. Said, B. Neubert, R. Měch, B. Benes, and O Deussen. 2012b. Plastic Trees: Interactive Self-adapting Botanical Tree Models. *ACM Trans. Graph.* 31, 4, Article 50 (July 2012), 10 pages.
P. Prusinkiewicz, M. Hammel, and E. Mjolsness. 1993. Animation of plant development. In *SIGGRAPH '93*. ACM Press, New York, NY, USA, 351–360.
P. Prusinkiewicz and Aristid Lindenmayer. 1990. *The Algorithmic Beauty of Plants*. Springer-Verlag New York, Inc.
E. Quigley, Y. Yu, J. Huang, W. Lin, and R. Fedkiw. 2018. Real-Time Interactive Tree Animation. *IEEE Trans. on Vis. and Comp. Graphics* 24, 5 (2018), 1717–1727.
A. Runions, M. Fuhrer, B. Lane, P. Federl, A. Rolland-Lagan, and P. Prusinkiewicz. 2005. Modeling and visualization of leaf venation patterns. *ACM Trans. Graph.* 24, 3 (2005), 702–711.
A. Runions, B. Lane, and P. Prusinkiewicz. 2007. Modeling Trees with a Space Colonization Algorithm. (2007), 63–70. https://doi.org/10.2312/NPH/NPH07/063-070
F. W. M. R. Schwarze, J. Engels, and C. Mattheck. 2000. *Fungal strategies of wood decay in trees*. Springer Science & Business Media.
H. Shao, T. Kugelstadt, T. Hädrich, W. Pałubicki, J. Bender, S. Pirk, and D. L. Michels. 2021. Accurately Solving Rod Dynamics with Graph Learning. In *NeurIPS*.
J. Spillmann and M. Teschner. 2007. CORDE: Cosserat Rod Elements for the Dynamic Simulation of One-Dimensional Elastic Objects. In *Eurographics/SIGGRAPH Symposium on Computer Animation*.
J. Spillmann and M. Teschner. 2008. Cosserat nets. *IEEE transactions on visualization and computer graphics* 15, 2 (2008), 325–338.
P. Tan, T. Fang, J. Xiao, P. Zhao, and L. Quan. 2008. Single Image Tree Modeling. *ACM Transactions on Graphics* 27, 5, Article 108 (2008), 7 pages.
A. N. Tikhonov. 1952. Systems of differential equations containing small parameters in the derivatives. *Matematicheskii sbornik* 73, 3 (1952), 575–586.
O. Šťava, S. Pirk, J. Kratt, B. Chen, R. Měch, O. Deussen, and B. Benes. 2014. Inverse Procedural Modelling of Trees. *Computer Graphics Forum* 33, 6 (2014), 118–131. https://doi.org/10.1111/cgf.12282
B. Wang, Y. Zhao, and J. Barbič. 2017. Botanical Materials Based on Biomechanics. *ACM Trans. Graph.* 36, 4, Article 135 (jul 2017), 13 pages.
H. Wang, Mengzhen Kang, J. Hua, and X. Wang. 2013. Modeling plant plasticity from a biophysical model: biomechanics. (11 2013).
J. Wither, F. Boudon, M.-P. Cani, and C. Godin. 2009. Structure from silhouettes: a new paradigm for fast sketch-based design of trees. *Comp. Graph. Forum* 28, 2 (2009), 541–550. https://doi.org/10.1111/j.1467-8659.2009.01394.x
S.-K. Wong and K.-C. Chen. 2015. A Procedural Approach to Modelling Virtual Climbing Plants With Tendrils. *Comput. Graph. Forum* (2015).
L. Yang, M. Yang, and G. Yang. 2019. Modeling fractures and cracks on tree branches. *Computers & Graphics* 80 (2019), 63–72.
Y. Zhao and J. Barbič. 2013. Interactive Authoring of Simulation-Ready Plants. *ACM Trans. Graph.* 32, 4, Article 84 (jul 2013), 12 pages.
X. Zhou, B. Li, B. Benes, S. Fei, and S. Pirk. 2023. DeepTree: Modeling Trees with Situated Latents. *IEEE Trans. on Vis. and Comp. Graphics* (2023), 1–14.

A Physical Invariance of the State Variables

A central design goal of our fungal wood decay model is that all internal state variables represent physical quantities: fungal activity, tissue health, defense concentration, and moisture. To remain under the premise of an interactive simulation, these quantities must stay within interpretable ranges under arbitrary user inputs, spatial heterogeneity, and long simulation times. The following result shows that this is not only enforced numerically but is an intrinsic property of the continuous model: the coupled reaction-diffusion system admits a forward-invariant *physical box* that coincides exactly with the intended normalization ranges used throughout the paper.

In order to prove this, assume homogeneous Neumann boundary conditions for all diffusing fields and initial data

$$R_w, R_b, H_c, H_l, C \in [0,1]\,, \qquad M \in [M_2, M_1] \quad \text{a.e. in } \Omega\,,$$

in which Ω is the solid region occupied by the dead wood. Then every sufficiently regular solution of the model equations satisfies, for all $t \geq 0$,

$$R_w, R_b, H_c, H_l, C \in [0,1]\,, \qquad M \in [M_2, M_1] \quad \text{a.e. in } \Omega\,.$$

Proof. The argument is a direct application of inward-pointing reaction terms and the parabolic maximum principle.

Fungal activity and defense. For $u \in \{R_w, R_b, C\}$, the reaction term used in the paper has the form

$$F(u,\cdot) = g(\cdot)\,u(1-u) - \lambda(\cdot)\,u\,, \qquad g, \lambda \geq 0\,,$$

or, equivalently for C, $F(0,\cdot) \geq 0$ and $F(1,\cdot) \leq 0$. Thus the vector field points inward on $[0,1]$. With no-flux boundary conditions, the maximum principle for reaction-diffusion equations implies $u(\cdot,t) \in [0,1]$ for all t.

Tissue health. The health variables satisfy pointwise linear kinetics

$$\partial_t H = -a(x,t)H + b(x,t)(1-H)\,, \qquad a, b \geq 0\,.$$

At $H = 0$ the time derivative is nonnegative, and at $H = 1$ it is nonpositive, so the interval $[0,1]$ is invariant at every spatial point.

Moisture. The moisture equation can be written as

$$\partial_t M = \nabla\cdot(D_M \nabla M) + (M_1 - M)k_{\text{in}} - (M - M_2)k_{\text{out}}\,, \qquad k_{\text{in}}, k_{\text{out}} \geq 0\,.$$

The source term satisfies $S(M_2) \geq 0$ and $S(M_1) \leq 0$, hence it pushes M inward at the endpoints. The maximum principle therefore yields $M(\cdot,t) \in [M_2, M_1]$.

Combining the three cases shows that the Cartesian product $[0,1]^5 \times [M_2, M_1]$ is forward invariant. □

B Mathematical Rationale for Transient Barrier Effects

The emergence of a barrier-active plateau follows from classical singular perturbation theory.

Proof. For sufficiently large κ and β, the coupled system admits a separation of timescales in which the defense variable C relaxes rapidly relative to the slow evolution of tissue health. By Tikhonov's theorem [1952], trajectories rapidly approach a normally attracting slow manifold defined by the algebraic constraint $\partial_t C = 0$, yielding the quasi-steady relation $C^*(R) = \frac{\kappa R}{\kappa R+\delta}$. Restricting the dynamics to this manifold reduces the effective fungal activity through the inhibited balance $\alpha H(1-R) \approx \beta C^*(R)$, implying an effective lignin decay rate $k_{\text{eff}} = \gamma_l R$ that decreases monotonically with both κ and β. Consequently, lignin health evolves exponentially slowly along the slow manifold, producing an extended interval of negligible mass loss. As tissue degradation progresses, defense inducibility weakens and the finite decay rate δ prevents permanent inhibition, leading to a loss of normal hyperbolicity [Fenichel and Moser 1971] and allowing trajectories to exit the inhibited regime and recover accelerated degradation. The observed plateau, therefore, corresponds to a parameter-controlled residence time near a defense-dominated slow manifold, whose duration increases monotonically with barrier strength. □

C Parameters and Performance Analysis

Table 1. Runtime statistics.

Figure	#Segments	Run Time (s)	Per-iteration time (s)
Fig. 6	108,395	20	0.135
Fig. 12	215,010	521	0.417
Fig. 13	215,010	347	0.417
Fig. 14	146,820	388	0.217
Fig. 15	72,015	44	0.137
Fig. 16	56,712	336	0.098
Fig. 19a	56,712	421	0.098
Fig. 19b	109,835	536	0.139
Fig. 19c	125,849	659	0.213

Table 2. Parameter variations

Figure	Parameter	Values
Fig. 6	Shrinkage gain for REG rest offsets in the radial (R) and tangential (T) directions. (S_R/S_T)	(a) 0.1 / 1 (b) 1 / 0.1 (c,d) 1 / 1
Fig. 16	Moisture bounds (M_1/M_2)	(a) 0.6 / 0.2 (b) 0.6 / 0.4
Fig. 11	#BSP cells	(a) 12800 (b) 5120 (c) 800 (d) N/A

Table 3. Model parameters, units, and meaning. All fields are defined on rod elements (REG nodes) unless stated otherwise.

Symbol	Unit	Description
Biophysical state		
R_w, R_b	–	White-/brown-rot activity, normalized to $[0,1]$.
H_c, H_l	–	Carbohydrate / lignin health fraction, normalized to $[0,1]$.
C	–	Defense efficacy, normalized to $[0,1]$.
M	kg/kg	Gravimetric moisture content.
M_1, M_2	kg/kg	Maximum / minimum admissible moisture. Typical values: 1.0, 0.1.
$M_{\text{min}}, M_{\text{max}}$	kg/kg	Moisture window for active fungal growth. Typical values: 0.2, 0.9.
s_t	kg/kg	Smoothstep width controlling how sharply growth turns on/off near M_{min} and M_{max} in Eq. 10. Typical value: 0.05.
Fungal growth and transport		
α_{w0}, α_{b0}	1/day	Baseline white-/brown-rot growth rates before moisture gating. Typical range: $[10^{-4}, 10^{-2}]$.
$\alpha_w(M), \alpha_b(M)$	1/day	Moisture-gated growth rates in Eq. 10.
D_w, D_b	m^2/day	Diffusion coefficients for R_w and R_b on the REG. Typical range: $[10^{-7}, 10^{-5}]$.
λ_l, λ_c	–	Weights of lignin / carbohydrate availability in white-rot growth. Typical values: 0.5, 0.5.
K_c	–	Half-saturation constant for carbohydrate accessibility in white rot. Typical value: 0.2.
β_w, β_b	1/day	Defense-mediated inhibition strengths in Eqs. (8), (9). Typical range: $[10^{-4}, 10^{-2}]$.
Health and defense		
γ_{cw}, γ_{cb}	1/day	Carbohydrate depletion rates by white / brown rot in Eq. 12. Typical range: $[10^{-4}, 10^{-2}]$.
γ_{lw}	1/day	Lignin depletion rate by white rot in Eq. 13. Typical range: $[10^{-4}, 10^{-2}]$.
ρ_c, ρ_l	1/day	Recovery gains driven by defenses in Eqs. 12–13. Typical range: $[10^{-5}, 10^{-3}]$.
κ	1/day	Defense induction gain in Eq. 14. Typical range: $[10^{-4}, 10^{-2}]$.
δ	1/day	Defense decay rate in Eq. 14. Typical range: $[10^{-6}, 10^{-4}]$.
D_C	m^2/day	Defense diffusion coefficient. Typical range: $[10^{-7}, 10^{-5}]$.
$\Pi(H)$	–	Tissue-condition modulation of defense inducibility; in our implementation, $\Pi(H) = H_c H_l$.
Moisture transport		
D_{M0}	m^2/day	Baseline moisture diffusivity. Typical range: $[10^{-6}, 10^{-4}]$.
$D_M(x,t)$	m^2/day	Health-dependent moisture diffusivity in Eq. 20.
k_{DM}	–	Sensitivity of D_M to health loss in Eq. (20). Typical range: $[0,1]$.
$k_{\text{in}}, k_{\text{out}}$	1/day	Moisture uptake / loss rate functions in Eq. 15; implemented as functions of bark distance $bd(x)$ and carbohydrate health H_c, with k_{in} increasing with H_c and decreasing with bd, and k_{out} varying oppositely.
$bd(x)$	m	Distance-to-bark field used in the moisture exchange term; static in the current implementation unless stated otherwise.
Moisture-to-mechanics coupling		
M_0	kg/kg	Drying threshold below which shrinkage and failure-limit updates are activated. Typical value: 0.2.
S	1/(kg/kg)	Shrinkage gain for REG rest offsets in Eq. 16. Typical range: $[0,1]$.
s	1/(kg/kg)	Shrinkage gain for rod rest length in Eq. 17. Typical range: $[0, 0.05]$.
L_0	–	Baseline strain limits (per constraint type).
$L(M)$	–	Moisture-scaled strain limits in Eq. 18.
p_ℓ	–	Exponent controlling the moisture-to-limit mapping in Eq. 19. Typical range: $[3,5]$.
Anisotropy and integrity		
(e_r, e_t, e_l)	–	Local radial / tangential / longitudinal wood frame used to evaluate anisotropic transport and the weak-point field.
$W(x)$	–	Specimen-specific weak-point field; implemented as a 3D Perlin noise evaluated in the local wood frame and used to modulate transport / growth coefficients.
θ_{ij}	–	BSP boundary indicator for REG edge (i,j); $\theta_{ij} = 1$ if edge (i,j) crosses a BSP cell boundary.
BSP size/depth	–	Binary-space-partition control parameter setting the coarse cuboid scale used for brown-rot prepatterning.
k_c, k_l	–	Integrity-loss gains from carbohydrate and lignin depletion in Eq. 21. Typical values: 1, 1.
I_{ij}	–	Edge integrity factor applied to REG connections in Eq. 21.
Contact and time stepping		
r_i	m	Capsule radius for rod segment i in contact handling. Typical range: $[0.005, 0.05]$.
k_{col}	N/m^2	Collision stiffness in penalty contact, Eq. 4. Typical value: 30.
μ_f	–	Friction coefficient in Eq. 7. Typical range: $[0.5, 1.0]$.
Δt	s	Mechanics time step used by XPBD/contact.
ε	m/s	Small velocity floor in the friction update.
Δt_{mech}	s	Mechanics step size (XPBD). Typical value: 0.01.
Δt_{bio}	day	Biophysical step size (forward Euler on the REG). Typical value: 0.5.
N_{mech}	–	Number of mechanics substeps per macro step. Typical value: 25.